

# Modeling of Plasma Processing Equipment - Current Trends and Challenges

Shahid Rauf<sup>a</sup>, Jason Kenney<sup>a</sup>, Zhigang Chen<sup>a</sup>, Kallol Bera<sup>a</sup>, Ankur Agarwal<sup>a</sup>,  
Ajit Balakrishna<sup>a</sup>, and Kenneth Collins<sup>a</sup>

<sup>a</sup>*Applied Materials, Inc.*  
974 E. Arques Ave., M/S 81517, Sunnyvale, CA 94085, USA

**Abstract.** Plasma modeling is a critical technology for the design of industrial plasma processing systems. Plasma processes are increasingly being extended to the sub-20 mTorr regime in the microelectronics industry, requiring accurate plasma models in the low pressure regime. Simultaneously, economic considerations are imposing stringent requirements on plasma uniformity over large substrates and plasma modeling is expected to address these uniformity challenges. These trends are necessitating good theoretical understanding in low temperature plasmas of (a) kinetic phenomena at low pressures and (b) the complex interplay between plasma, electromagnetic, chemical and fluid dynamics phenomena in three dimensions. Several fluid and particle-in-cell models are used in this paper to address issues of importance to the design and use of plasma etching and deposition systems.

**Keywords:** Plasma modeling, plasma processing, particle-in-cell plasma model, fluid plasma model

**PACS:** 52.65.-y, 52.77.-j

## INTRODUCTION

Due to the growing complexity of industrial plasma processing systems and technological requirements for plasma processes becoming more stringent, plasma modeling has become a critical technology for the design of these systems in recent years. Plasma processing is increasingly being done in the sub 20-mTorr regime where kinetic effects become important. Many aspects of these low pressure plasma systems remain poorly understood and existing kinetic plasma models are inadequate to address industrial design needs. Simultaneously, uniformity control requirements are becoming stringent in plasma processing equipment with advancing microelectronics technologies. While some aspects of plasma uniformity can be dynamically controlled during plasma processing (e.g., by varying the inter-electrode gap [1]), careful reactor design determines the fundamental uniformity limits achievable in a given plasma processing system. Three-dimensional (3D) plasma models that can examine the inter-coupling between different physical phenomena in the plasma are essential for the design of next generation plasma processing systems. Several kinetic and fluid plasma models are described in this paper that take into consideration the inter-coupling between plasma dynamics, electromagnetics, fluid flow, and plasma chemistry. These models are used to understand electron heating and power dissipation mechanisms in low pressure capacitively coupled plasmas, elucidate the sources of plasma non-uniformities, and develop uniformity improvement techniques.

## COMPUTATIONAL MODELS

The results in this paper have been generated using three separate computational models. Our first 3D fluid plasma model [2, 3] includes the continuity and momentum conservations equations for all species and the Maxwell equations in their potential formulation. The equation governing the vector potential,  $\mathcal{A}$ , is solved in the frequency domain after each cycle. The coupled set of equations governing the scalar potential,  $\phi$ , and transport equations for all charged species are solved implicitly in time. The model also includes the electron energy conservation equation.

The effect of static magnetic field can be included through the charged species transport properties, which become tensor quantities in the presence of a static magnetic field. We will refer to this model as the *fluid plasma model* in the remainder of this paper.

The second 3D model [4, 5] includes the coupled set of Maxwell equations and transport equations for all species, which are solved explicitly in time. The Maxwell equations are discretized using the finite-difference time-domain (FDTD) method. The plasma model includes the time-dependent continuity equations for charged and neutral species, drift-diffusion approximation for specie fluxes, and the electron energy conservation equation. This model, labeled as the *plasma-FDTD model*, allows us to self-consistently account for the inter-coupling between the plasma and the external RF system.

Our third model [6] uses the well-established particle-in-cell (PIC) technique for simulating charged species. Details of the computational methodology can be found in Ref. [7] and the model includes a Monte Carlo based model for charged species collisions. Since multiple neutral species are present in plasmas of typical etching gases, the PIC model is coupled to a fluid model for neutral species that takes into account specie transport in the plasma bulk, chemical reactions, and surface processes.

## COMPUTATIONAL RESULTS

We first apply the fluid plasma model to investigate the influence of an exposed asymmetric feature surrounding the lower electrode in a capacitively coupled plasma (CCP) system [8]. The basic plasma processing system geometry is illustrated in Fig. 1(a). The top electrode is 40 cm in diameter and is surrounded by a quartz ring providing a dielectric break between the upper electrode and the grounded chamber body. The bottom electrode is 30 cm in diameter, surrounded by a thin silicon ring set within another quartz ring. The top and bottom electrodes are 7.5 cm apart. A grounded metal shell around the lower electrode completes the assembly. The chamber wall has an inner diameter of 50 cm. The pump port connecting the wall to the metal shell is assumed to be a perforated metal plate and is also grounded.

We consider an exposed asymmetric feature surrounding the lower electrode, in this case a thin off-axis circular plate. In all cases, the asymmetric plate is a cylinder 5 mm thick, extending 5 mm beyond the grounded shell on one side at the symmetry plane. On the other side it ranges from 5 mm to 35 mm beyond the shell, giving separations between chamber and plate axes of 0 to 15 mm and minimum gaps between plate and chamber wall of 4 cm down to 1 cm. Both grounded metal and quartz plates are considered.

The plasma is generated using a 13.56 MHz generator connected to the bottom electrode. The top electrode is grounded. The operating conditions are 500 W RF power and 100 mTorr gas pressure in Ar for all simulations. As shown in Fig. 1(a), where a symmetric grounded plate extends 5 mm outside the metal shell, these conditions result in electron density peaking near the edge of the bottom electrode. The off-center electron density peak is due to electric field enhancement at the bottom electrode edge. In addition, with the large gap between plate and chamber wall, the plasma spreads into the region below the plate.

In Figs. 1(b-d), time-averaged electron density profiles resulting from three asymmetric grounded plate geometries are shown. In each plot, density and chamber geometry are truncated at a position 2.5 cm above the lower electrode, where the electron density peaks for all cases. In Fig. 1(b), relative to the symmetric discharge in Fig. 1(a), the peak density is seen to shift toward the region where the plate is larger, here extending a maximum of 15 mm beyond the shell. This trend continues in Fig. 1(c), where the maximum annular plate thickness is 25 mm. Here, however, the plasma has begun to be squeezed out where the gap between the plate and wall narrows to 2 cm. Finally, in Fig. 1(d), the gap narrows to 1 cm and the plasma here is confined to the region above the plate. The peak density in turn shifts 80° away from this area, where the gap has increased to 2.25 cm.

To explain this behavior, one needs to consider the grounded surface area 'visible' to the plasma with each plate design, as the RF current from the bottom electrode returns to ground through these surfaces (along with the top electrode). With moderate increases in the plate size, the combined area of the plate and chamber wall (even below the plate level) is available for current collection. Thus, the location where the gap between plate and wall reaches a minimum receives the highest current and in turn the highest plasma densities result. On the other hand, an extreme narrowing of the gap prevents the plasma from leaking into the region below the plate, reducing current flow to that region as the effective grounded surface area has decreased. The peak density then shifts away to a location where the plasma is not confined.

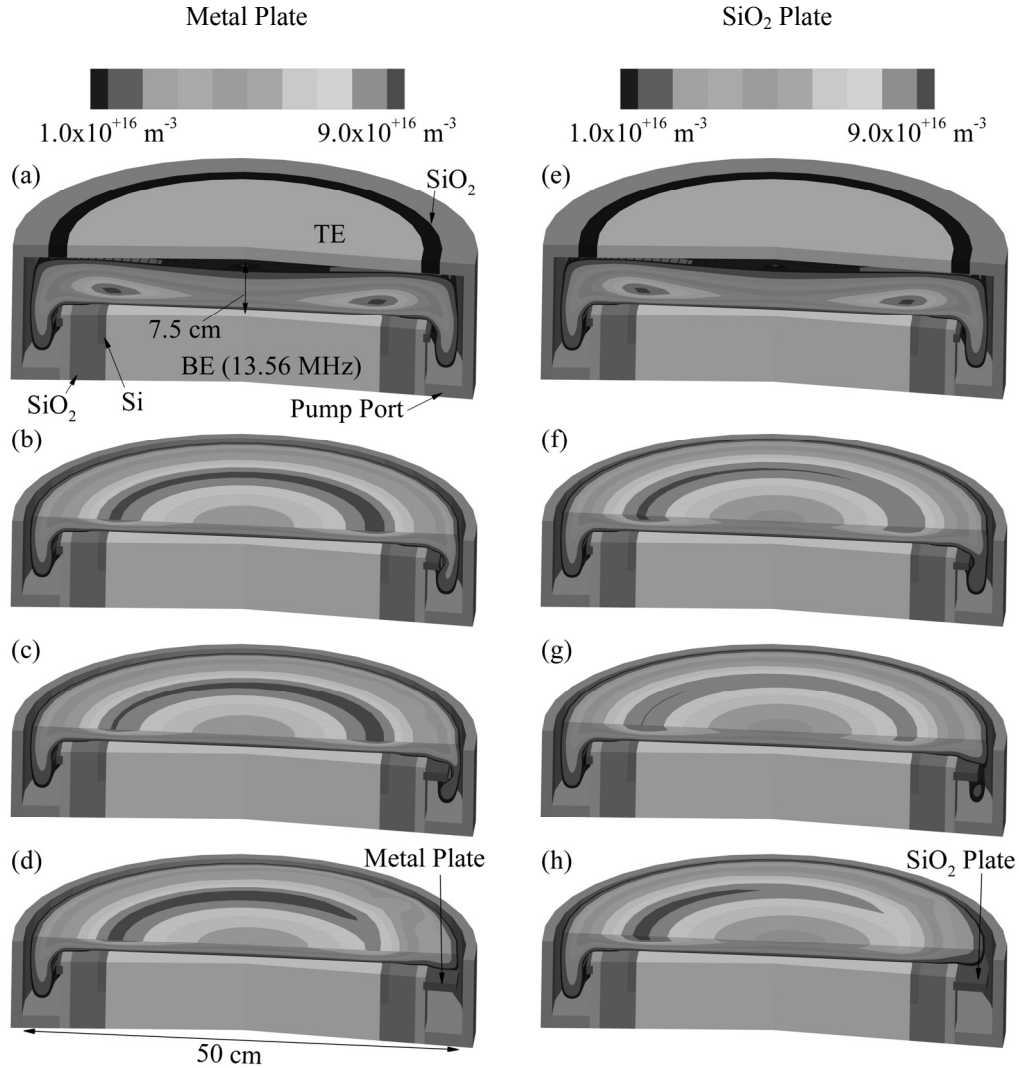


**FIGURE 1.** Time-averaged electron density profiles for grounded metal and  $\text{SiO}_2$  plates. Maximum width of metal plate is (a) 5 mm (uniform), (b) 15 mm, (c) 25 mm, and (d) 35 mm. Maximum width of  $\text{SiO}_2$  plate is (e) 5 mm (uniform), (f) 15 mm, (g) 25 mm, and (h) 35 mm. Plot is truncated in (b)-(d) and (f)-(h) at level of peak density. The operating conditions are 500 W RF power and 100 mTorr gas pressure in Ar.

When using a quartz plate, an opposite trend occurs, as shown in Figs. 1(e-h). Time-averaged electron density profiles are plotted for the same four plate geometries, this time truncated 3 cm above the bottom electrode, as the peak location has shifted slightly upward. Here, the axisymmetry of Fig. 1(e) gives way to increasingly non-uniform distributions in Figs. 1(f-h). In Figs. 1(f) and (g), the peak densities decrease, as plasma is able to leak into the region below the plate at all locations and the effect is that of lengthening current pathways. The electron density peak is opposite to the location with the widest plate, as the quartz plate shadows the region underneath it from the RF current, effectively reducing the grounded area visible to the plasma. In Fig. 1(h), the plasma is confined above the plate in the region where the gap is narrowest, resulting in a more dramatic shift in plasma density to the side with large gap. The peak density is now also larger than that of the axisymmetric case, as more current is funneled to the side with large gap due to the blocking of current pathways opposite.

We next use the fluid plasma model to investigate the effect of a static magnetic field on the characteristics of a CCP discharge [3]. We consider an Ar discharge generated using a very high frequency (VHF) RF source in the chamber geometry shown in Fig. 2(a), where all hardware components are axi-symmetric. The top and bottom electrodes are spaced 7.5 cm apart and a 162 MHz VHF source is connected to the top electrode. The top electrode

is separated from the grounded chamber wall using a quartz ring, and the gas outlet is assumed to be a dielectric boundary with  $\epsilon_r = 1$ . A 5 nF blocking capacitor is connected between the bottom electrode and ground.

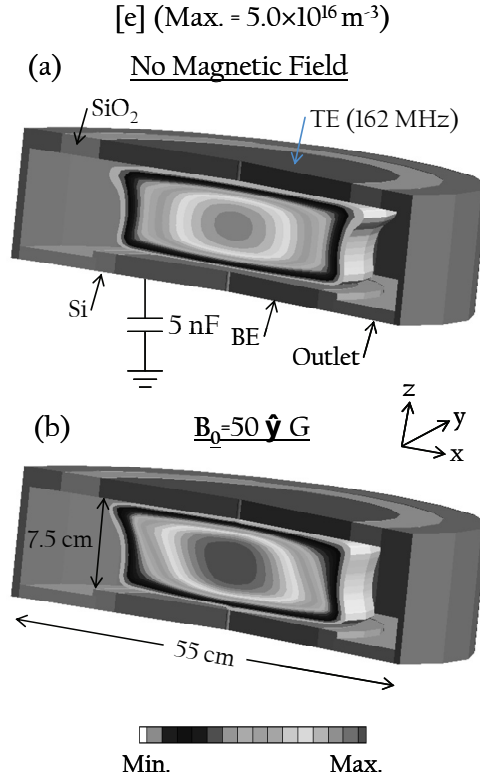


**FIGURE 2.** The electron density (a) without magnetic field and (b) with  $B_0 = 50 \hat{y}$  G. The conditions are 200 W applied at 162 MHz from the top electrode and 100 mT gas pressure in Ar.

Electron density with and without a static magnetic field is shown in Fig. 2 for 200 W (162 MHz) RF power and 100 mTorr gas pressure in Ar. The magnetic field in Fig. 2(b) is 50 G and is assumed to be in the +y direction. Without the magnetic field, the plasma discharge is axisymmetric and electron density peaks in the center of the chamber. Plasma concentrates in the chamber's radial center due to the well-known standing electromagnetic wave effect at the VHF frequency considered [9]. The large inter-electrode gap further enhances electromagnetic power deposition in the chamber center relative to power deposition at top electrode edge. As the plasma is concentrated in the chamber center, it is expected that the RF current coming in through the top electrode primarily flows out through the bottom electrode and the plasma discharge is electrically almost symmetric. Consequently, sheath voltage and thickness is commensurate at the top and bottom electrodes.

Plasma characteristics change considerably with the application of the magnetic field. First, for the same RF power, electron density is substantially larger due to electron confinement in the direction perpendicular (z) to the magnetic field and electrodes. Second, the plasma shifts in opposite directions ( $\pm x$ ) adjacent to the top and bottom electrodes. This plasma shift is due to the well-known  $\mathbf{E} \times \mathbf{B}$  drift [10]. As the DC electric field is largest in the sheath regions next to the electrodes, the  $\mathbf{E} \times \mathbf{B}$  drift is dominant in the sheath and pre-sheath regions. Also, because of the electrically symmetric nature of the discharge, the  $\mathbf{E} \times \mathbf{B}$  drift is commensurate at both electrodes. The drift occurs in opposite directions ( $\pm x$ ) at the two electrodes as the DC sheath electric field is in opposite directions at the top (+z) and bottom (-z) electrodes.

We next examine the electrical and plasma behavior of a large area CCP reactor as a function of frequency. The plasma-FDTD model is used in this investigation. The simulations have been conducted in the plasma reactor geometry shown in Fig. 3. The inter-electrode spacing in the plasma chamber is 3 cm. The bottom electrode has a size of  $3.05 \text{ m} \times 2.85 \text{ m}$ , which represents the size of Gen 10 substrates in the flat panel display industry. An RF power source is connected at the top, which is coupled to the plasma chamber through an air-filled transmission line of rectangular cross section. There is a Teflon dielectric ring between the top electrode and the sidewall. The

frequencies we choose expand both the HF and VHF ranges: 13.56 MHz, 27 MHz, 40 MHz, 60 MHz, 100 MHz, and 200 MHz. We apply 20-kW RF power to the reactor shown in Fig. 3 at these frequencies. The gas pressure is set to 2 Torr in  $H_2$ .

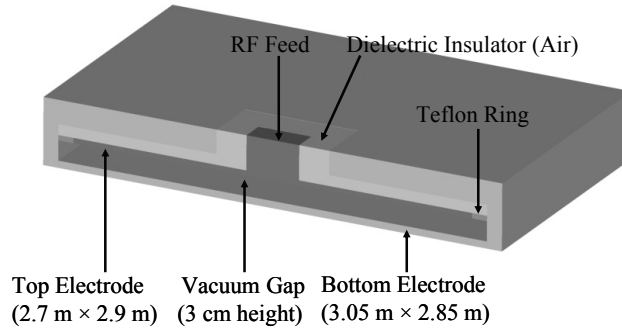


FIGURE 3. The large-area plasma reactor.

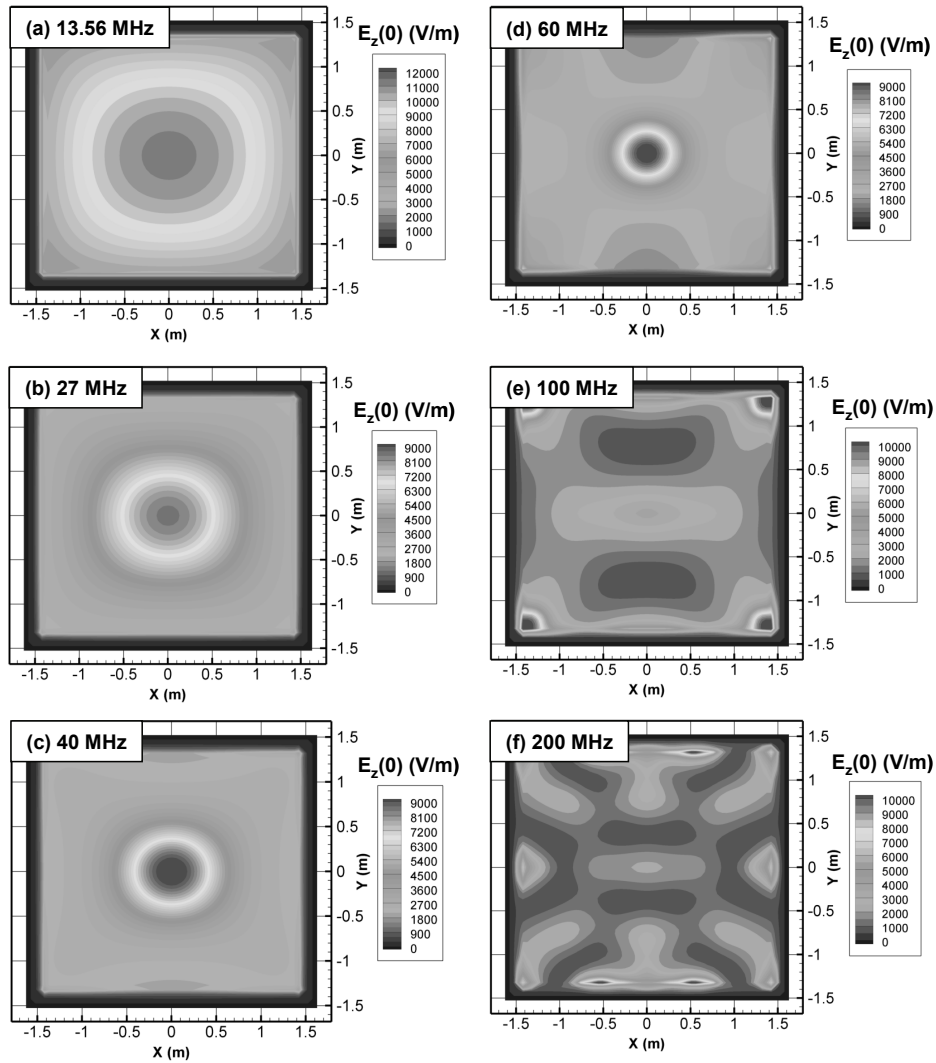
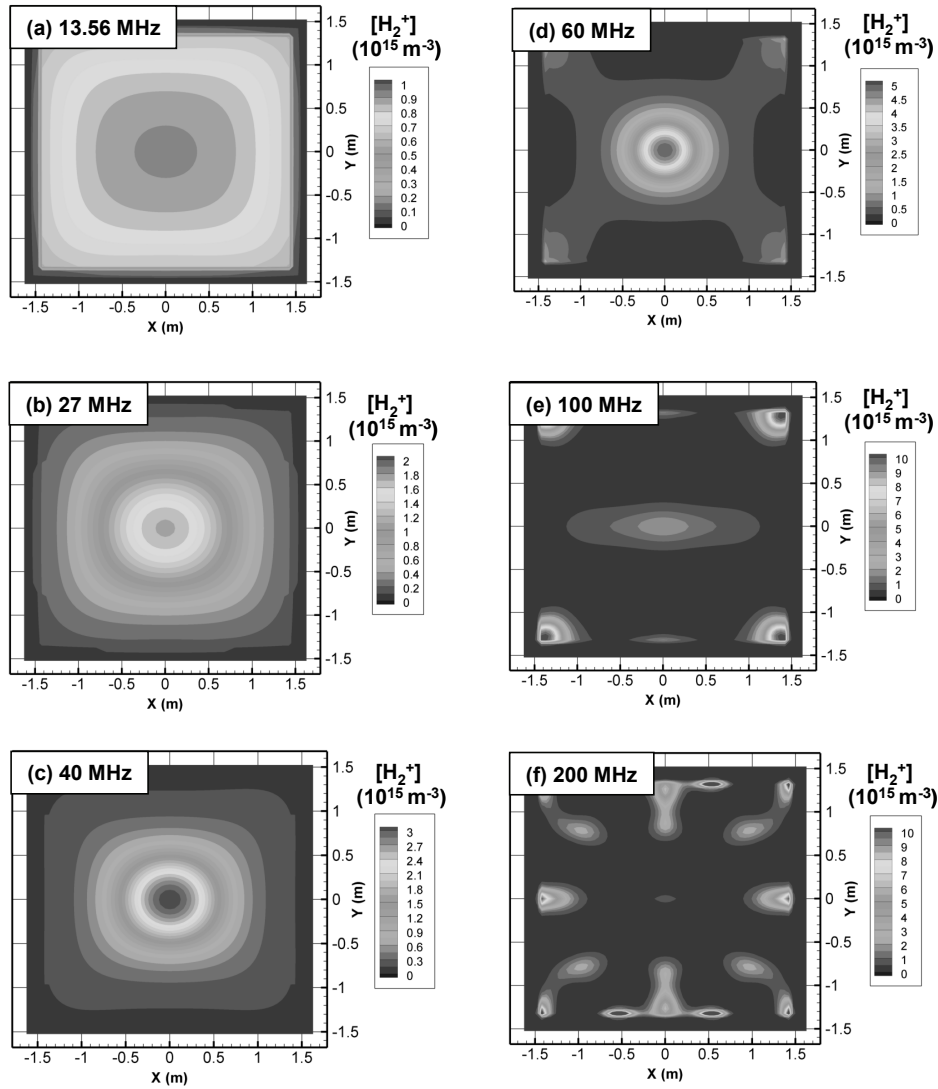


FIGURE 4. Magnitude of the 0<sup>th</sup> harmonic of electric field in the top plasma sheath. The operating conditions are  $H_2$  at 2 Torr, and 20 kW at (a) 13.56, (b) 27, (c) 40, (d) 60, (e) 100, and (f) 200 MHz.



**FIGURE 5.** The spatial distribution of  $\text{H}_2^+$  density in the middle of the inter-electrode gap. The  $\text{H}_2^+$  density is normalized to  $10^{15} \text{ m}^{-3}$ . The operating conditions are  $\text{H}_2$  at 2 Torr, and 20 kW at (a) 13.56, (b) 27, (c) 40, (d) 60, (e) 100, and (f) 200 MHz.

Figure 4 shows the horizontal distribution of the magnitude of the time-averaged electric field  $[E_x(0)]$  in the top plasma sheath at each frequency. At 13.56 MHz, the electric field peaks at the center of the chamber due to the interference of the incident and reflected electromagnetic waves in the reactor that results in a standing wave pattern. Such a standing wave pattern has been reported in previous publications [2, 9]. From Fig. 4, we see that the peak of the electric field at the center becomes sharper as the frequency is gradually increased from 13.56 MHz to 60 MHz. Clearly, as the frequency increases, the electrical wavelength decreases, and the electric field gradient increases given the fixed chamber dimensions. Therefore, the electric field behaves like being “squeezed” more to the center. However, it should be noted that at 40 MHz and 60 MHz, electric field tends to get higher at the four corners as well. Such behavior is not observed at 13.56 MHz and 27 MHz. This behavior is significantly enhanced at 100 MHz where the peak of the electric field completely shifts from the center to the four corners, and the center instead has a moderate level of electric field. Furthermore, we see some low field spots between the corners and the center. The low-field spots are particularly pronounced in the  $y$  direction along which the electrode has a smaller dimension. The low-field spots between the corners and the center and high fields at corners are the signatures of higher-order rectangular harmonics. At 200 MHz, even higher-order rectangular harmonics come into play, and the electric fields show more complex pattern with multiple field peaks along the edges.

Focusing on the plasma, Fig. 5 shows the normalized horizontal  $H_2^+$  distribution in the middle of the inter-electrode gap. The spatial distribution of  $H_2^+$  resembles that of the electric field at the corresponding frequencies, showing similar standing wave patterns determined by various orders of rectangular harmonics. Due to the large electrode size, small inter-electrode gap and high gas pressure, the plasma at each location is representative of the local power deposition characteristics, which is clearly linked to the electric field. However, due to the nonlinear dependence of the ionization rate on electron temperature or power deposition, the gradient of  $H_2^+$  looks shaper than that of the corresponding electric field. The peak density of  $H_2^+$  increases from  $9.2 \times 10^{14} \text{ m}^{-3}$  to  $1.7 \times 10^{16} \text{ m}^{-3}$  as the frequency increases from 13.56 MHz to 200 MHz. This increase is due to more localized nature of the plasma and more efficient plasma production at higher frequencies.

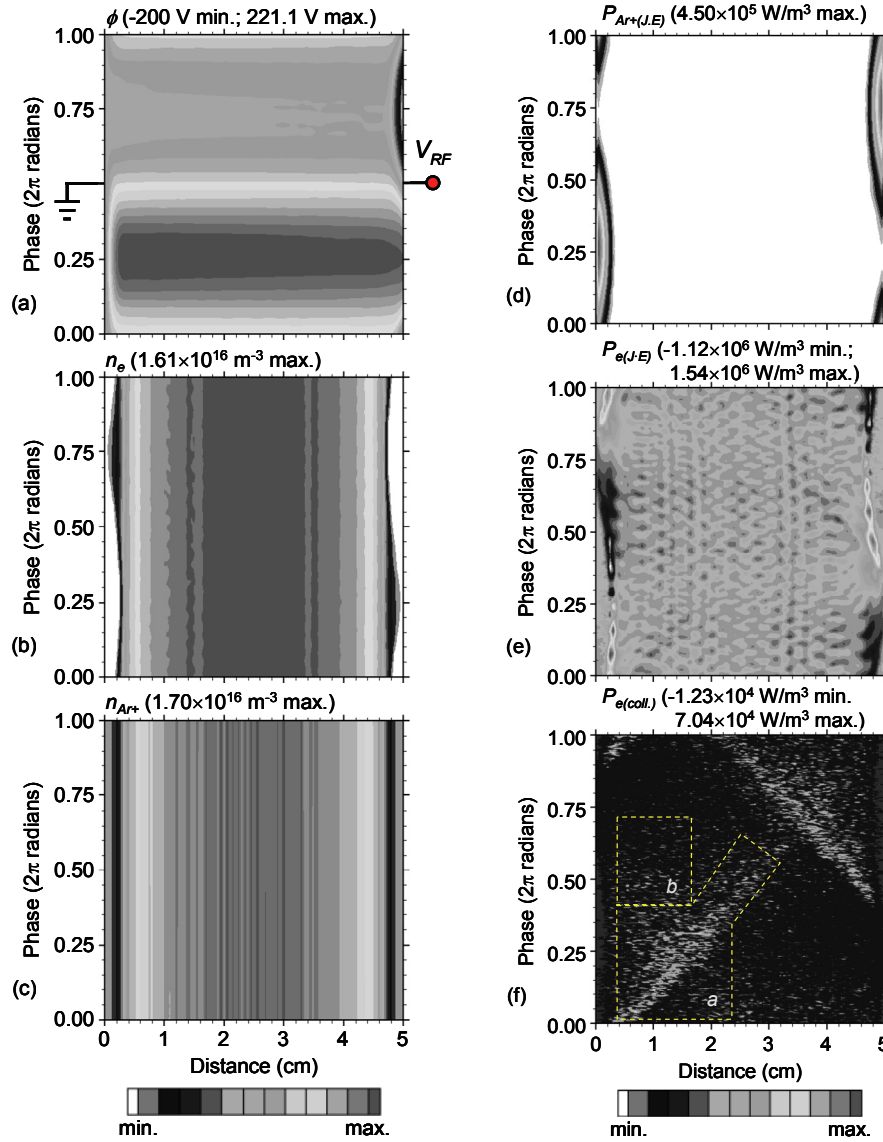


**FIGURE 6.** (a) The electrical potential, (b) the electron density, (c) the  $Ar^+$  density, (d)  $Ar^+$  power absorption from the electric field, (e) electron power absorption from the electric field and (f) electron power loss through collisions as a function of phase during 1 RF cycle and distance between the two electrodes. The operating conditions are 20 mTorr in Ar, and 200 V at 60 MHz applied to the right electrode.

In the last problem, we use the PIC model to understand how electrons and ions gain and lose energy in a parallel plate CCP [6]. In the simulation, the secondary electron emission coefficient for ions is 0.3 on both electrodes, the

inter-electrode gap is 5 cm, RF voltage is 200 V at 60 MHz, and the gas is Ar. The electrical potential, the electron density and the Ar<sup>+</sup> density are shown in Figs. 6(a-c) as a function of distance between the electrodes ( $y$ ) and phase during the RF cycle. The RF voltage is applied to the right electrode, while the left electrode is grounded. During the first half of the RF cycle, applied voltage is positive and this voltage primarily drops across the sheath at the left electrode. With the sheath almost collapsing adjacent to the right electrode, electrons are pulled towards the positively biased right electrode. The situation reverses during the second half of the RF cycle where the sheath voltage is large at the right electrode and electrons are attracted to the left electrode. Because the positive ions are massive, ion density does not change significantly during the RF cycle. The ion density is non-negligible in the sheath regions.

Focusing on the power dynamics, we have shown the power adsorbed by Ar<sup>+</sup> and electrons from the electric field ( $\mathbf{J}\cdot\mathbf{E}$ ) and power electrons lose during collisions in Figs. 6(d-f). Since the potential is generally negative at both electrodes with respect to the plasma potential, positive ions are lost from the plasma to the electrodes and consume energy during acceleration in the sheaths. As shown in Fig. 6(d), Ar<sup>+</sup> ion power absorption is highest at the left sheath during the first half of the RF cycle (when the sheath voltage drop is largest there) and at the right sheath during the second half. Based on the results in Fig. 6(e), electrons gain energy from the electric field at the edge of the sheath when the sheath expand into the plasma and pushes the electrons towards the plasma. Electrons however return some of the power back to the electric field (negative  $\mathbf{J}_e\cdot\mathbf{E}$ ) when the sheaths contract and electrons diffuse in towards the electrodes. Some of the negative power absorption is also due to beam electrons (from the opposite sheath) slowing down in the sheath. Secondary electrons are generated at the electrode surfaces and accelerate towards the plasma.

The energy that electrons gain during sheath expansion is not dissipated at the sheath edge but, as shown in Fig. 6(f), energetic electron beams shoot into the plasma bulk and the electrons lose their energy over a considerable distance extending into the plasma bulk (region a). Once the sheath stops expanding, there is a phase (region b) when secondary electrons generated at the electrode surface are the primary source of electron collision energy loss in the plasma.

## CONCLUSIONS

In conclusion, particle-in-cell and 3D fluid plasma models have been used to understand issues of relevance to the design of industrial plasma processing systems. It was shown that azimuthally-asymmetric reactor components introduce azimuthal perturbations in the plasma due to asymmetric RF current return path. Similarly, magnetic fields can distort the plasma due to the  $\mathbf{E} \times \mathbf{B}$  drift. As the reactor dimensions become large, electromagnetic effects can make the plasma non-uniform. Finally, a PIC model was used to illustrate how electrons lose and gain energy in low pressure CCPs and its influence on the plasma spatial distribution.

## REFERENCES

1. K. Bera, S. Rauf, K. Ramaswamy, and K. Collins, *J. Vac. Sci. Technol. A* **27**, 706-711 (2009).
2. S. Rauf, K. Bera, and K. Collins, *Plasma Source Sci Technol.* **17**, 035003 (2008).
3. S. Rauf, J. Kenney, and K. Collins, *J. Appl. Phys.* **105**, 103301 (2009).
4. S. Rauf, Z. Chen, and K. Collins, *J. Appl. Phys.* **107**, 093302 (2010).
5. Z. Chen, S. Rauf, and K. Collins, submitted to *J. Appl. Phys.*
6. S. Rauf, K. Bera, and K. Collins, *Plasma Sources Sci Technol.* **19**, 015014 (2010).
7. C. K. Birdsall and A. B. Langdon, *Plasma Physics via Computer Simulation*, Bristol: IOP Publishing, 1991.
8. J. Kenney, S. Rauf, and K. Collins, *J. Appl. Phys.* **106**, 103302 (2009).
9. M. A. Lieberman, J. P. Booth, P. Chabert, J. M. Rax, and M. M. Turner, *Plasma Sources Sci. Technol.* **11** 283-293 (2002).
10. F. F. Chen, *Introduction to Plasma Physics and Controlled Fusion* 2<sup>nd</sup> Ed. (Plenum Press, New York, 1984). Pg. 19